Euler-Poincaré Characteristic and Invasion Percolation for Critical Radius Determination: A Systematic Comparison in Synthetic Porous Structures

Resumen

La determinación del radio crítico (R_c) en medios porosos es esencial para la estimación de permeabilidad mediante modelos analíticos. Este estudio presenta la primera comparación sistemática del método de la Característica de Euler-Poincaré (EPC) y el algoritmo de Percolación por Invasión basado en cola de prioridad (QBIP) utilizando cuatro estructuras porosas sintéticas (SPS) con geometría y topología controladas para determinar R_c. QBIP demostró aplicabilidad universal, determinando R_c = 0.09–0.15 µm en todas las SPS. EPC requirió conectividad inicial negativa para su aplicación; valores positivos impidieron la identificación del cruce por cero, y aunque el criterio de derivada detectó transiciones en la distribución de tamaño de poro (PSD), estas no corresponden a umbrales de percolación en estructuras desconectadas. Las desviaciones respecto a las modas de diseño variaron entre 0–70% para EPC y 6.7–50% para QBIP; ningún criterio fue uniformemente superior. A pesar de que las operaciones morfológicas alteraron la PSD inicial para lograr la porosidad objetivo en la generación de SPS, ambos métodos identificaron R_c dentro del mismo orden de magnitud que las modas de diseño (0.10–0.15 µm). Estos hallazgos demuestran que EPC y QBIP proporcionan perspectivas complementarias: EPC revela transiciones topológicas mientras QBIP

captura la física de invasión, permitiendo la caracterización geométrica, topológica y capilar de medios porosos. Este enfoque dual proporciona criterios cuantitativos para la selección del método basados en la conectividad de la muestra y permite la validación cruzada para reducir la incertidumbre en la determinación de R_c para su uso en modelos analíticos de permeabilidad.

Abstract

Critical radius (R_c) determination in porous media is essential for permeability estimation through analytical models. This study presents the first systematic comparison of the Euler-Poincaré Characteristic (EPC) method and queue-based Invasion Percolation (QBIP) algorithm using four synthetic porous structures (SPS) with controlled geometry and topology to determine R_c. QBIP demonstrated universal applicability, determining R_c = 0.09–0.15 μm across all SPS. EPC required negative initial connectivity for its application; positive values prevented zero-crossing identification, and while the derivative criterion detected pore size distribution (PSD) transitions, these do not correspond to percolation thresholds in disconnected structures. Deviations from design modal radii ranged from 0–70% for EPC and 6.7–50% for QBIP; no single criterion was uniformly superior. Despite morphological operations altering the initial PSD to accomplish the target porosity in SPS generation, both methods identified R_c within the same order of magnitude as the design modes (0.10–0.15 μm). These findings demonstrate that EPC and QBIP provide complementary insights: EPC reveals topological transitions while QBIP captures invasion physics, enabling geometric, topological, and capillary

characterization of porous media. This dual-method approach provides quantitative criteria for the selection of the method based on sample connectivity and enables cross-validation to reduce uncertainty in R_c determination for use in analytical permeability models.

Keywords

Permeability, Critical radius, Invasion Percolation, Euler-Poincaré Characteristic, Digital Rock Physics

Palabras clave: Permeabilidad, Radio crítico, Percolación por Invasión, Característica de Euler-Poincaré, Física de Roca Digital

Nomenclature

k, Permeability, (md)

Z, Coordination number

l, Characteristic length

H, Connectivity factor

χ, Euler-Poincaré Characteristic number

χ_0, Initial EPC value (at r = 0)

β_0, Number of connected components

β_1, Number of independent loops

β_2, Number of enclosed cavities

ϕ, Porosity (fraction)

r, Pore-throat radius (μm)

r_{max}, Largest available pore-throat (μm)

P_c, Capillary pressure (Pa)

γ, Interfacial tension (N/m)

θ, Contact angle (degrees)

R_c, Critical radius (μm)

R_{WGM}, Weighted geometric mean radius (μm)

R_{apex}, Apex radius (μm)

S, Saturation (fraction)

n, Number of evaluation radii

$P(r)$, Pore space after morphological opening at radius r

$B(r)$, Spherical structuring element of radius r

77 $d(p)$, EDT value at pore voxel p (μm)

78 r_{design}, Design modal radius (μm)

79 $\%dev$, Percentage deviation from design modal radius (%)

80

81

82

83

84

85

86

87

88

89

90

91

92

93

94

95

96

97

98

99

Glossary

EPC, Euler-Poincaré Characteristic method

QBIP, Queue-Based Invasion Percolation algorithm

IBIP, Image-Based Invasion Percolation algorithm

SPS, Synthetic Porous Structures

PSD, Pore Size Distribution

PTSD, Pore-Throat Size Distribution

DRP, Digital Rock Physics

DRM, Digital Rock Modeling

MICP, Mercury Intrusion Capillary Porosimetry

NMR, Nuclear Magnetic Resonance

BPC, Bundle of Parallel Capillaries

MDC, Multidirectional Channels

HTN, Hierarchical Tree Network

DCN, Degree-Constrained Network

EDT, Euclidean Distance Transform

WEM, Water Expulsion Method

micro-CT, X-ray micro-computed tomography

1. Introduction

The study of porous media is relevant for many industrial applications, particularly oil and gas extraction. Reservoir management requires accurate characterization of rock properties for optimal drainage point selection, production rate optimization, completion and perforation design, and enhanced oil recovery strategies (Ahmed, 1991). One intrinsic property that controls fluid flow through reservoir rocks is absolute permeability (hereafter referred to as permeability). This property can be expressed through the scaling relation (Bernabé et al., 2010):

$$k = Hl^2, \tag{1}$$

where H is a connectivity factor that depends on the microstructural characteristics of the medium, e.g., porosity, fractal dimensions, tortuosity (Ghanbarian et al., 2013), coordination number (Z), and formulations derived from various theoretical frameworks (Bernabé et al., 2010; Rezaee, 2012; Li et al., 2016; Daigle, 2016; Bernabé et al., 2016), and l is a characteristic length. Permeability k has units of m² (SI) or millidarcys (md) in petroleum engineering applications. In percolation theory, critical path analysis (Katz & Thompson, 1986, 1987; Hunt, 2001) establishes that pore throats control macroscopic flow, with conductances exceeding a critical threshold. In this context, l corresponds to the critical radius (R_c), defined as the representative pore-throat radius at the percolation threshold — when continuous fluid pathways first connect opposite faces of the porous medium.

When direct permeability measurements such as well tests or permeameter analyses (Spivey & Lee, 2013; McPhee et al., 2015) are not available, Eq. 1 provides

an alternative for its estimation. Determining both H and l becomes essential. While establishing H is beyond the scope of this study, multiple studies have successfully used R_c as the characteristic length l in this framework (Bernabé, 1995; Arns et al., 2005; Daigle, 2016; Robins et al., 2016; Nishiyama & Yokoyama, 2017; Zhao et al., 2019). Experimentally, R_c can be estimated through mercury intrusion capillary porosimetry (MICP) (Katz & Thompson, 1986; Amann-Hildenbrand et al., 2013; Franco-Villegas et al., 2025) or gas breakthrough experiments such as the water expulsion method (WEM) (Hildenbrand et al., 2002; Nishiyama & Yokoyama, 2017). However, experimental methods present limitations, including sample alteration, extended equilibration times, and lack of three-dimensional (3D) spatial information (León y León, 1998; Amann-Hildenbrand et al., 2013; Rashid et al., 2015). These challenges motivate the development of computational approaches for determining R_c from digital images of rocks.

The Digital Rock Physics (DRP) paradigm utilizes rock images to simulate physical processes (Andrä et al., 2013a, 2013b; Blunt et al., 2013; Kelly et al., 2015). Although DRP allows estimation of permeability (Kelly et al., 2015; Aguilar-Madera et al., 2020) using numerical approaches to solve Navier-Stokes equations (Narsilio et al., 2009; Mostaghimi et al., 2013; Guibert et al., 2016; Verri et al., 2017), or Lattice Boltzmann (Kelly et al., 2015; Bultreys et al., 2016; Santos et al., 2022), the use of computational resources is extensive, depending on the porous space computational domain, limiting its applicability (Mostaghimi et al., 2013; Blunt et al., 2013; Bultreys et al., 2016).

Within this paradigm, two computational methods have emerged as alternatives for R_c determination from 3D images. The first approach is rooted in the Minkowski functionals framework, which provides a set of morphological measures to quantify pore structure (Vogel et al., 2010). Among these functionals, the Euler-Poincaré Characteristic (hereafter referred to as EPC) quantifies connectivity changes through topological analysis (Vogel, 1997; Vogel et al., 2002; Zhao et al., 2019; Armstrong et al., 2019). Chaniot et al. (2022) extended this approach to quantify morphological accessibility on stochastic models using the full set of Minkowski functionals. The second approach employs invasion percolation algorithms that simulate fluid displacement processes (Hilpert & Miller, 2001; Gostick, 2022). This study implements the Image-Based Invasion Percolation (IBIP) algorithm using the priority-queue-based variant (QBIP) (Gostick, 2024), selected for its computational efficiency and open-source implementation in the PoreSpy package (Gostick et al., 2019). Despite the application of both methods, no systematic comparison has been conducted to establish their relative performance, operational limits, and convergence conditions for R_c estimation.

Part of DRP is the Digital Rock Modeling (DRM) discipline for generating computational representations of rocks (Roth et al., 2011). Methods include process-based approaches simulating geological processes (Zhu et al., 2012; Luo et al., 2020), multiple-point statistics (Okabe & Blunt, 2005), and machine learning techniques (Mosser et al., 2017). However, for method validation, realistic reconstruction introduces complexity and uncertainty. When evaluating EPC and QBIP capabilities, the requirement is not geological realism but precise control of

microstructure (Zhu et al., 2012). Synthetic Porous Structures (SPS) provide this control, serving as phantoms with deliberately designed geometries and known properties (Kaczmarek et al., 2017; Goral & Deo, 2020). This established validation approach (Jiang et al., 2013; Jivkov et al., 2013; Raeini et al., 2017; Armstrong et al., 2019) enables systematic parameter variation while maintaining ground truth. To allow comparison between EPC and QBIP, four SPS were designed from a bundle of parallel capillaries to degree-constrained networks, preserving full 3D morphological complexity at voxel resolution for direct image-based analysis. Figure 1 summarizes the relationships between these approaches.

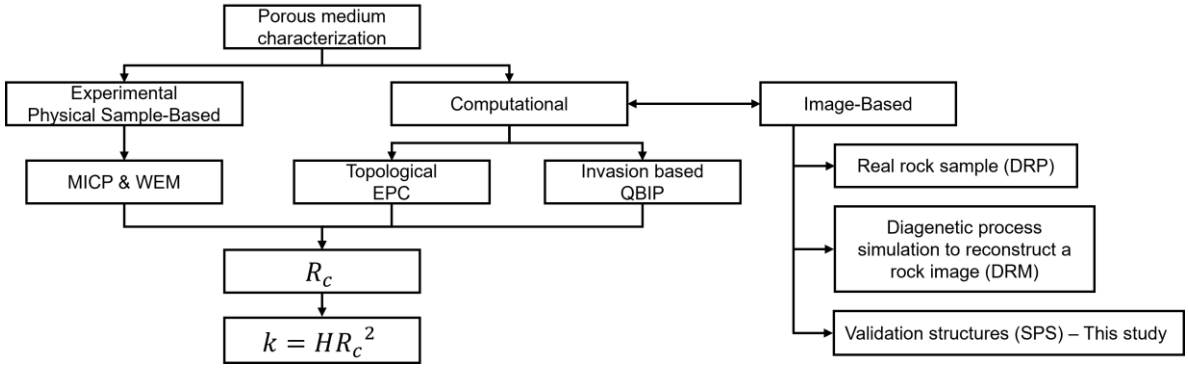

Figure 1. Conceptual framework for R_c determination in porous media. Two characterization approaches: experimental methods (MICP, WEM) operating on physical samples, and computational methods (EPC, QBIP) operating on 3D binary images. Within the Digital Rock Physics (DRP) paradigm, these images are obtained from real rocks or generated through Digital Rock Modeling (DRM). Synthetic Porous Structures (SPS), used in this study, provide controlled geometry for method validation. The characteristic length l in the permeability model $k = Hl^2$ corresponds to the critical radius R_c.

This study provides a controlled comparison between topological (EPC) and invasion-based (QBIP) approaches for R_c determination, identifying the conditions under which each method is applicable. The specific objectives are: (i) to quantify the agreement between EPC and QBIP methods across four SPS with varying topology, and (ii) to evaluate whether one EPC criterion (zero-crossing or derivative) shows consistently better agreement with invasion percolation results.

This article is organized as follows: Section 2 presents the theoretical foundations of percolation theory and the mathematical basis for both computational methods. Section 3 describes the SPS generation and the implementation details of EPC and QBIP algorithms. Section 4 presents the comparative results and discussion. Section 5 summarizes the conclusions and future research directions.

2. Theoretical framework

2.1. Geometric and topological measures of porous media

Porous media structure can be characterized through two complementary perspectives: geometric measures that quantify size and shape, and topological measures that characterize connectivity.

One of the representations of an interconnected porous medium consists of pore bodies connected by pore throats. Pore bodies (hereafter pores) provide storage capacity, while pore throats control fluid flow. Characterization of the pore network requires both geometric and topological measures.

2.1.1. Geometric characterization: size distributions

The irregular morphology of pores and pore-throats in porous materials can be quantitatively described through size distributions that provide statistical descriptors of their characteristic dimensions. The pore size distribution (PSD) is defined as the probability density of the pore radii within a given volume of porous medium, capturing the spatial variability of the void space responsible for fluid storage (Patmonoaji et al., 2020). In contrast, the pore-throat size distribution (PTSD) represents the statistical distribution of the narrow constrictions that connect adjacent pores, which governs pore connectivity and fluid flow across the network (Nelson, 2009; Xu et al., 2019). These constrictions typically act as flow-limiting elements, exerting control on percolation thresholds and the continuity of fluid pathways. Together, PSD and PTSD provide a geometric framework that links pore-scale morphology to permeability (Vogel et al., 2002). Figure 2 illustrates the distinction and complementarity between PSD and PTSD.

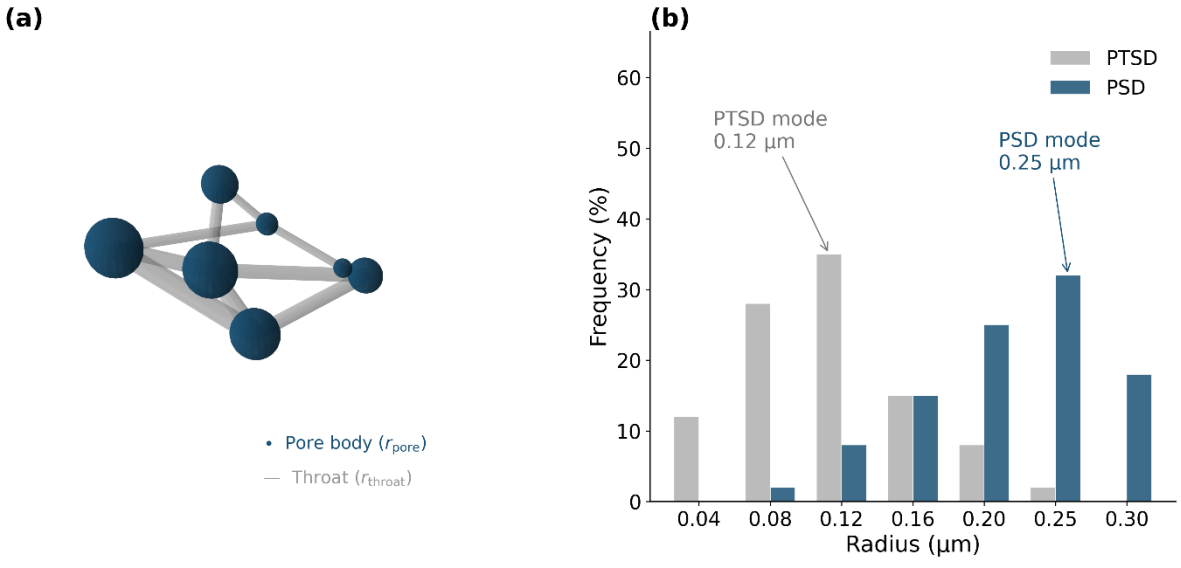

Figure 2. Schematic representation of PSD and PTSD in an interconnected porous medium. Pore radii define the PSD, while the narrow constrictions connecting adjacent pores define the PTSD.

To translate these geometric concepts into measurable quantities, various experimental and computational techniques have been developed. Among them, MICP remains one of the most widely used methods for estimating PTSD (Hou et al., 2025; Quan et al., 2025; Zhang et al., 2025). MICP produces PTSD through the relationship between invasion pressure and pore-throat radius (Giesche, 2006), providing valuable information on the pore-throat size distribution, entry pressure threshold, and cumulative porosity. PTSD is particularly relevant for determining the characteristic length scale l in permeability models, where pore-throat radii constrain permeability.

Alternatively, nuclear magnetic resonance (NMR) provides non-invasive estimations of pore size distribution (PSD) based on the relaxation times of hydrogen nuclei within saturated pore spaces, which correlate with pore radii (Arns et al., 2004; Zhang et al., 2016; Morales et al., 2025). While NMR does not directly image pore-throat geometry, advanced interpretation of relaxation data can provide indirect insight into pore-throat connectivity, particularly in systems with complex pore structures (Ghomeshi et al., 2018; Zheng et al., 2018; Huang et al., 2020).

Conversely, X-ray micro-computed tomography (micro-CT), with spatial resolution typically in the micrometer range, when combined with segmentation algorithms (e.g., watershed or deep learning), enables direct 3D reconstruction of porous

networks. This allows extraction of both PSD and PTSD by identifying individual pores and their connecting pore-throats (Patmonoaji et al., 2020; Guo et al., 2024; Hou et al., 2025). These image-derived pore networks can subsequently be used in pore network models to simulate flow, thereby linking microscopic geometry to macroscopic permeability (Raeini et al., 2017; Ma et al., 2025).

2.1.2. Topological characterization

The topology quantifies the way the pores and the pore throats are connected (Sahimi, 2011). For this study, two topological descriptors are particularly relevant, the Z and the Betti numbers.

Z quantifies the average number of pore throats connected to each pore (Rabbani & Jamshidi, 2016). Higher Z values indicate greater connectivity and enhanced permeability (Bernabé et al., 2010). This parameter is relevant for generating SPS.

The Betti numbers quantify topological features in different dimensions on the global scale. For 3D porous media, the first three Betti numbers suffice to characterize connectivity (Sahimi, 2011; Robins et al., 2016). These combine to form the Euler-Poincaré Characteristic (χ), which quantifies overall network connectivity through:

$$\chi = \beta_0 - \beta_1 + \beta_2 \,, \tag{2}$$

where β_0 is the number of connected components, β_1 is the number of independent loops, and β_2 is the number of enclosed cavities (Vogel et al., 2010). For porous media, $\chi < 0$ indicates multiply-connected structures with redundant pathways, $\chi =$

279 0 represents marginal connectivity, and $\chi > 0$ means disconnected or simply-
280 connected structures.

281 2.2. Invasion percolation

282 Invasion percolation describes a dynamic process fundamentally different from
283 ordinary percolation (Wilkinson & Willemsen, 1983). While ordinary percolation
284 theory considers static accessibility, where all pores with radius $r > r_{threshold}$
285 become simultaneously available (pressure or size-controlled process)—invasion
286 percolation models a sequential displacement process between defending and
287 invading fluids (volume or rate-controlled invasion) (Gostick, 2022).

288 In this representation, pores and pore throats initially contain defending fluid
289 (Knackstedt & Paterson, 2009). When injection occurs at infinitesimal flow rates
290 where capillary forces dominate viscous effects, the dynamics follow local pore-
291 throat dimensions. During drainage—the displacement of wetting by non-wetting
292 phases—capillary resistance concentrates at the narrowest constrictions: the pore
293 throats. The displacement therefore proceeds through discrete jumps across the
294 pore throats, with the non-wetting phase advancing through the largest available
295 opening that offers the least resistance (Knackstedt & Paterson, 2009).

296 This mechanism produces self-organized invasion patterns distinct from random
297 percolation (Wilkinson & Willemsen, 1983), naturally identifying the flow pathways
298 that control network connectivity.

Invasion percolation and image-based porosimetry via morphological opening both approximate quasi-static drainage, representing volume-controlled and pressure-controlled protocols, respectively (Hilpert & Miller, 2001; Gostick et al., 2024). The relationship between capillary pressure P_c (Pa) and pore-throat radius r (m) follows the Young-Laplace equation (Washburn, 1921):

$$P_c = \frac{2\gamma cos\theta}{r}, \quad (3)$$

where γ is the interfacial tension (N/m) and θ is the contact angle (degrees). For practical reporting, capillary pressures were converted to psi (1 psi = 6,895 Pa) and pore-throat radii are expressed in micrometers (μm) throughout this study.

2.3. Critical radius determination

Experimentally, R_c can be determined by multiple approaches. In MICP tests, R_c corresponds to the inflection point of the invasion curve, identified as the maximum of $dS/dlog(r)$, which represents the modal radius of the PTSD (Katz & Thompson, 1986; Comisky et al., 2007; Amann-Hildenbrand et al., 2013; Franco-Villegas et al., 2025). This modal radius indicates the pore-throat radius class that contributes most significantly to mercury saturation when percolation occurs. Similarly, the WEM provides direct observation of the percolation threshold: R_c is determined when the first gas bubble emerges at the opposite face of the sample, with the corresponding pressure converted to radius via Eq. 3 (Nishiyama & Yokoyama, 2017).

These experimental observations reveal fundamental characteristics of R_c . First, its correspondence with the PTSD mode indicates that R_c represents the most abundant pore-throat radius in the PTSD capable of forming continuous pathways, not simply the largest throats, but those numerous enough to establish connectivity across the sample. If the PTSD differs from a nominal or design distribution (e.g., due to morphological modifications; see Section 3.1), the measured mode—and therefore R_c—shifts accordingly. Second, this modal behavior explains why R_c controls percolation: these throats offer minimal capillary resistance while being sufficiently abundant to connect two external and opposite faces. Once this critical pressure is exceeded, progressively smaller throats ($r < R_c$) become accessible, expanding the flowing fraction of the pore network and increasing permeability beyond the threshold value (Hildenbrand et al., 2002).

3. Materials and methods

3.1. Synthetic porous structures

SPS with known properties are required to quantify and compare the performance of EPC and QBIP methodologies. Four 3D SPS were designed to evaluate both methods across different topological complexities, following the principle that these structures can serve as validation models for real rocks (Kaczmarek et al., 2017).

All SPS were generated within cubic domains of 7.5 × 7.5 × 7.5 μm³ with voxel resolution of 0.05 μm. Two pore size distributions were employed. MDC, HTN, and

DCN share a trimodal PSD with diameters of 0.8 μm (10%), 0.4 μm (30%), and 0.2 μm (60%), yielding a design modal radius of 0.10 μm. BPC uses a trimodal PSD with diameters of 0.5 μm (20%), 0.3 μm (50%), and 0.15 μm (30%), yielding a design modal radius of 0.15 μm. Design radii in Table 1 reflect voxel discretization (0.05 μm resolution) μm. The term "pore size" encompasses both pores and pore throats, as generation algorithms typically do not discriminate between these features (Roth et al., 2011).

After placement of pores and connecting structures, porosity fell below the target in MDC, HTN, and DCN (3.4%, 2.7%, and 3.7%, respectively). A single binary dilation (face-connected structuring element, 1 iteration) was applied to each, increasing porosity to 5.9%, 4.4%, and 6.7%. BPC required no morphological adjustment (final porosity 5.7%). The dilation added voxels at the periphery of existing pores without creating new pores or connections. The resulting porosities (4.4–6.7%) were selected as a representation of tight rock microstructures. Figure 3 shows the 3D pore structure before and after adjustment.

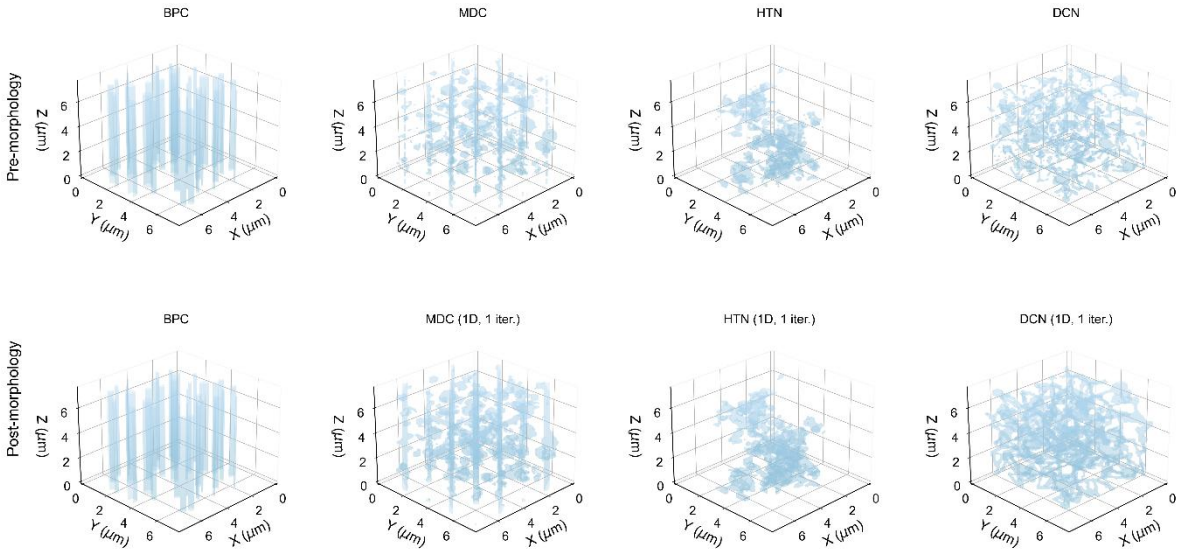

353

354 **Figure 3.** 3D visualization of the four SPS before (top) and after (bottom)
355 morphological adjustment. (a) BPC, (b) MDC, (c) HTN, (d) DCN.

356 The four SPS represent a systematic progression in network connectivity (Figure 3):
357 (a) Bundle of Parallel Capillaries (BPC) — non-intersecting cylindrical channels
358 traversing the domain independently; (b) Multidirectional Channels (MDC) —
359 orthogonal channels intersecting at the domain center with diagonal connections; (c)
360 Hierarchical Tree Network (HTN) — network constructed via Prim's minimum
361 spanning tree algorithm with branching; (d) Degree-Constrained Network (DCN) —
362 network where each pore has a target coordination number (large: 4–6, medium: 3–
363 4, small: 2–3). For graph-theoretic details, the reader is referred to Saha Ray, 2013.
364 This progression from disconnected parallel structures (χ_0 = 40) to highly connected
365 networks (χ_0 = −216) enables evaluation of how topology affects R_c determination.

366 Table 1. Structural properties of each SPS.

SPS	Graph type	Design radii (μm)	Fractions (%)	Modal r (μm)	χ_0	ϕ_{pre} (%)	ϕ_{pos} (%)	Operation
BPC	Forest (disconnected)	0.25/0.15/0.08	20/50/30	0.15	40	5.7	5.7	None
MDC	Connected grid	0.40/0.20/0.10	10/30/60	0.10	-15	3.4	5.9	1D (1 iter.)
HTN	MST with branches	0.40/0.20/0.10	10/30/60	0.10	-127	2.7	4.4	1D (1 iter.)
DCN	Degree-constrained	0.40/0.20/0.10	10/30/60	0.10	-216	3.7	6.7	1D (1 iter.)

3.2. Euclidean Distance Transform

The Euclidean Distance Transform (EDT) assigns to each pore voxel the minimum distance to the nearest solid boundary:

$$d(p) = \min_{s \in S} \|p - s\|, \quad (4)$$

where p represents a pore voxel position, S is the set of all solid voxels, and $\|\cdot\|$ denotes the Euclidean norm. This transform provides the inscribed sphere radius at each voxel (Hilpert & Miller, 2001) defining the range of pore radii used by both the EPC morphological opening loop (Section 3.3) and the QBIP invasion algorithm (Section 3.4).

3.3. EPC implementation

In 3D digital images, the EPC is computed using the Euler formula (Vogel et al., 2010):

$$\chi = n_{vertices} - n_{edges} + n_{faces} - n_{volumes}, \quad (5)$$

where the n symbol denotes 'number of'. For binary pore space images, each 2 × 2 × 2 voxel neighborhood contributes to the global χ value based on its specific configuration of pore and solid voxels. Eq. 5 provides the computational form of Eq. 2 for voxelized images.

The implementation used in this study computes χ using the scikit-image library (van der Walt et al., 2014). This topological measure proves particularly valuable when tracked as a function of pore radius, as discussed in the following section.

3.3.1. Connectivity function

The connectivity function $\chi(r)$ measures the Euler-Poincaré Characteristic as a function of pore radius. The approach was originally proposed by Vogel (1997) for serial sections of soils and formalized in Vogel (2002): a morphological opening with a spherical structuring element of radius r is applied to the pore space, and Eq. 5 is evaluated on the resulting opened domain $P(r)$ at each radius, yielding $\chi(r)$.

The implementation employs morphological opening, defined as erosion followed by dilation with a spherical structuring element $B(r)$ of radius r:

$$P(r) = (P \ominus B(r)) \oplus B(r), \tag{6}$$

where $\ominus$ denotes erosion and $\oplus$ denotes dilation. This operation removes all pore regions narrower than 2r—constrictions that cannot accommodate a sphere of radius r—while restoring the original dimensions of wider regions (Vogel, 1997; 2010).

The $\chi(r)$ curve is computed by applying Eq. 6 at n radii uniformly distributed between 0 and r_{max}, evaluating χ (Eq. 5) on each opened domain $P(r)$. Figure 4 summarizes this workflow.

3.3.2. Critical radius identification criteria

The determination of R_c from connectivity functions requires robust criteria that can handle diverse structures. This section presents two complementary criteria applied to SPS.

Zero-crossing criterion: The primary criterion defines R_c as the point where the connectivity function crosses zero (Vogel et al., 2010; Zhao et al., 2019):

$$R_c^{zero} = \{r : \chi(r) = 0\}, \quad (7)$$

This zero-crossing point is invariant under volume normalization, yielding identical R_c values for both $\chi(r)$ and $\chi_v(r)$=$\chi(r)/V_{sample}$.

However, this criterion has a limitation: in low-porosity media (ϕ < 10%), the pore network may become fragmented, causing χ_v to remain positive throughout the entire radius range. This behavior was observed in Eagle Ford shale samples where χ ≈ 9400, indicating poor connectivity even at the smallest radii (Davudov et al., 2020).

Derivative criterion: Analogous to the inflection point analysis in MICP (Amann-Hildenbrand et al., 2013; Franco-Villegas et al., 2025), the derivative of the connectivity function identifies the radius of most rapid topological transition. R_c is determined as:

$$R_c^{deriv} = \arg\max_r \left| \frac{d\chi(r)}{dr} \right|, \quad (8)$$

where the maximum absolute value captures the steepest transition regardless of sign.

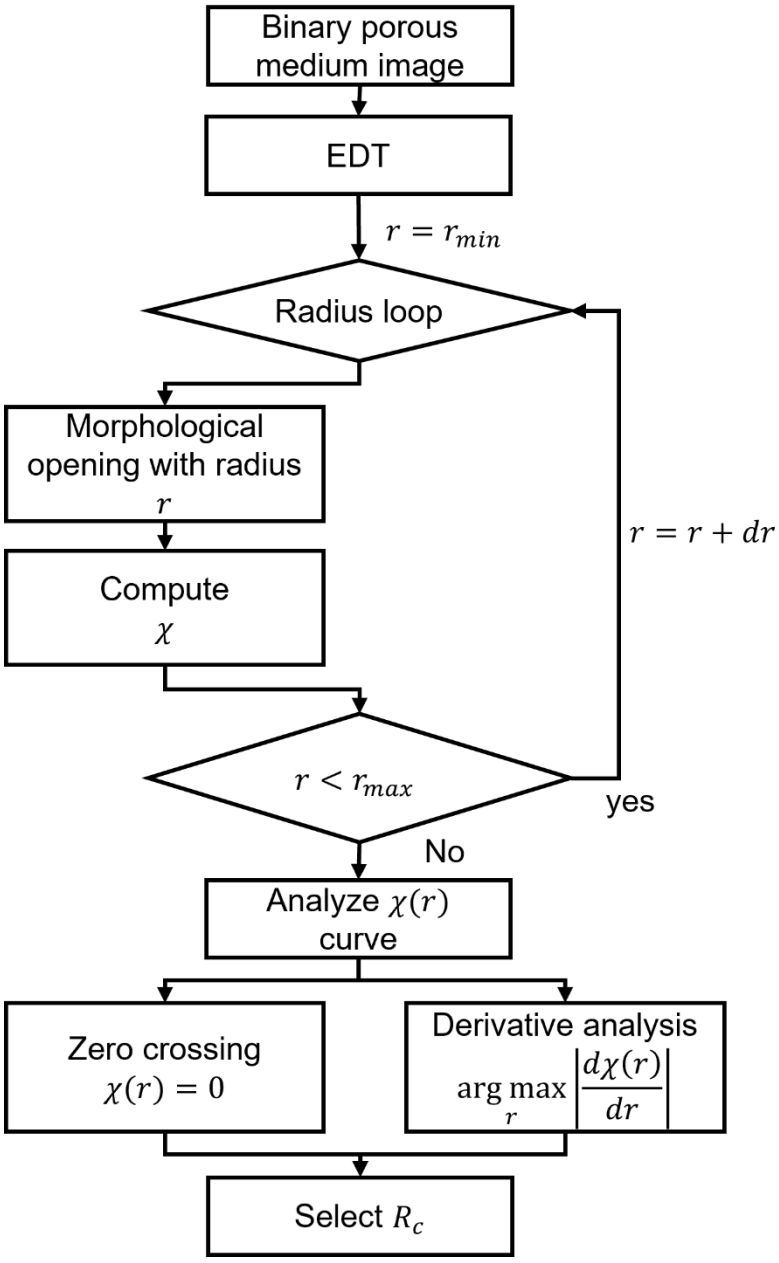

Figure 4. Workflow for R_c determination using the EPC. The algorithm iteratively applies morphological opening operations at increasing radii to compute the connectivity function $\chi(r)$. Two complementary criteria—zero-crossing and derivative criterion—are evaluated to identify the R_c.

3.4. QBIP algorithm implementation

QBIP simulates quasi-static drainage by computationally replicating capillary-controlled displacement in segmented 3D porous media. The algorithm leverages EDT to characterize pore space morphology (Hilpert & Miller, 2001), advancing the invasion interface through the pore-throat with minimum capillary entry pressure at each step. Implementation was performed in Python using the PoreSpy package (Gostick et al., 2019).

The algorithm implements volume-controlled invasion by incrementally filling fixed volumes (Gostick, 2022). Figure 5 illustrates the core invasion loop. This study adopts water-air interface properties: interfacial tension γ = 0.078 N/m and contact angle θ = 180° (non-wetting), enabling direct comparison with experimental drainage curves.

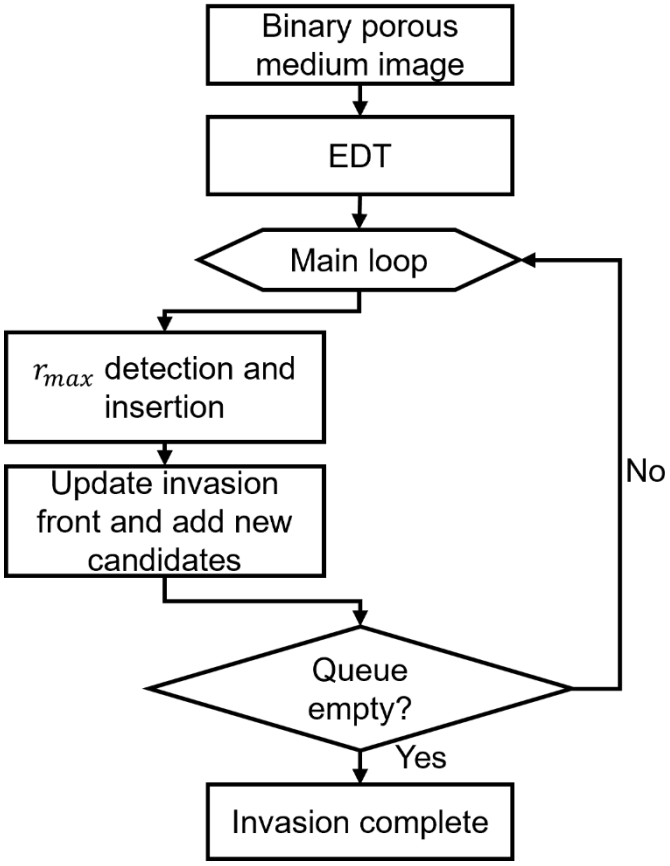

Figure 5. Core invasion loop of the QBIP algorithm. Starting from a binary image and its EDT, the algorithm iteratively selects r_{max} at the invasion front and inserts spheres at these locations. The candidate queue is updated through morphological dilation until it is empty, generating the complete invasion sequence.

3.4.1. Capillary pressure curve reconstruction

The non-wetting phase saturation (S) is defined as the fraction of connected pore volume (V_{pore}) occupied by the invading fluid. For each invasion step *i*, the saturation increment is:

$$\Delta S_i = \frac{(V_i - V_{i-1})}{V_{pore}} * 100\%, \tag{9}$$

where V_i is the cumulative invaded volume (in voxels) at step i. The pore-throat radius r_i at each step is obtained from the EDT value at the newly invaded voxels.

The invasion sequence yields two representations. The volume-controlled curve (Figure 6a) plots S versus r in invasion order, displaying capillary pressure fluctuations as the fluid traverses pore-throat constrictions and fills pores. The pressure-controlled reconstruction proceeds in two stages: first, invasion events are grouped into logarithmic bins by EDT-based radius, yielding the saturation contribution per radius class (Figure 6b); then, the bins are sorted from largest to smallest radius and their contributions are accumulated via:

$$S(r) = \sum_{r_i \geq r} \Delta S_i \times 100\%, \tag{10}$$

producing the stepped $S(r)$ curve and its derivative $dS/dlog(r)$, analogous to pressure-based intrusion experiments (Figure 6c).

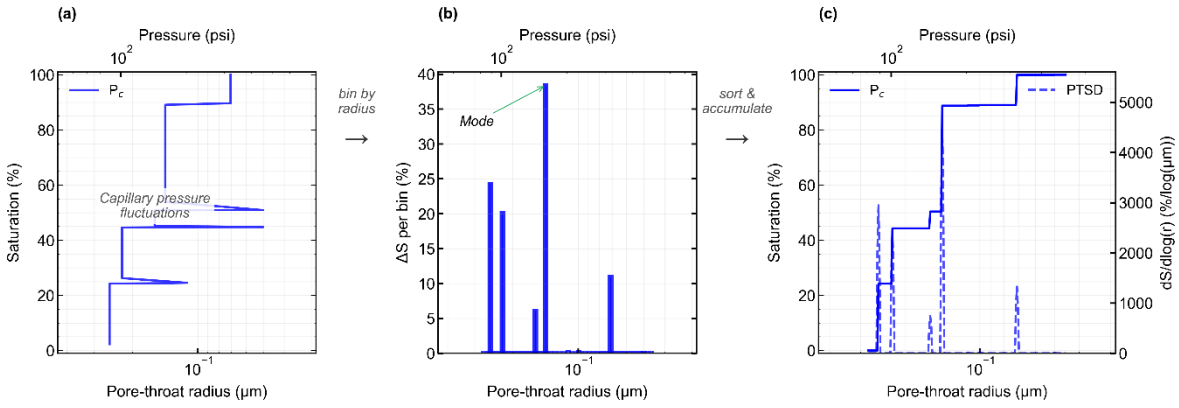

Figure 6. QBIP post-processing pipeline illustrated with BPC data. (a) Volume-controlled invasion curve showing capillary pressure fluctuations at pore-throat

breakthroughs. (b) Invasion events grouped into logarithmic bins by EDT-based radius. (c) Pressure-controlled reconstruction: cumulative saturation S(r) with PTSD.

3.4.2. Characteristic radii

The reconstructed capillary pressure curve and the binned saturation data enable R_c identification through two approaches: direct modal analysis of binned saturation data and derivative analysis of the reconstructed capillary pressure curve. Unlike EPC's topological analysis, QBIP tracks the evolution of fluid distribution during invasion.

Critical Radius: The percolation threshold corresponds to the PTSD maximum (Amann-Hildenbrand et al., 2013):

$$R_c = \arg\max_r \left(\frac{dS}{d\ log(r)}\right), \quad (11)$$

Modal contribution method: The modal method identifies R_c as the radius class with maximum saturation contribution:

$$R_c^{modal} = \arg\max_r \sum_{i \in bin(r)} \Delta S_i, \quad (12)$$

Apex Radius: Following Pittman's graphical method, the apex radius (R_{apex}) represents the threshold for continuous flow path formation (Pittman, 1992).

Weighted Geometric Mean Radius: This radius (R_{WGM}) captures the contribution of the entire pore-throat spectrum, particularly relevant for tight lithologies where pore-throat radii are dimensionally similar (Dastidar et al., 2007). Figure 7 represents the workflow for QBIP implementation used in this study.

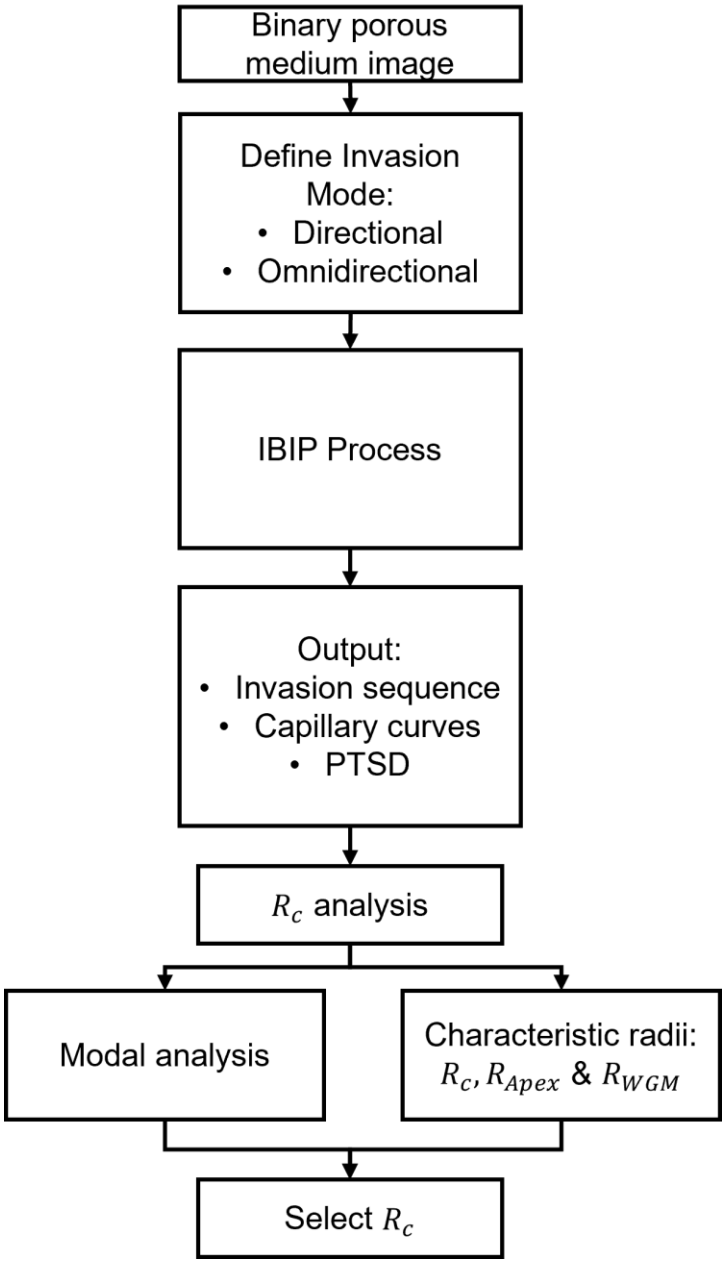

479

480 **Figure 7.** Methodological framework for critical radius determination using QBIP.
481 The algorithm operates in directional mode (invasion from a specified boundary),
482 generating the invasion sequence and enabling reconstruction of the capillary
483 pressure curve. Analysis proceeds through two paths: direct modal analysis of

binned data and derivative analysis of the reconstructed curve, both converging to R_c while the latter additionally yields R_{apex} and R_{WGM}.

4. Results and discussion

The four SPS were analyzed using both EPC analysis and QBIP invasion simulation to determine R_c values and method convergence conditions.

4.1. Bundle of parallel capillaries

The BPC structure contained parallel capillaries without lateral connections.

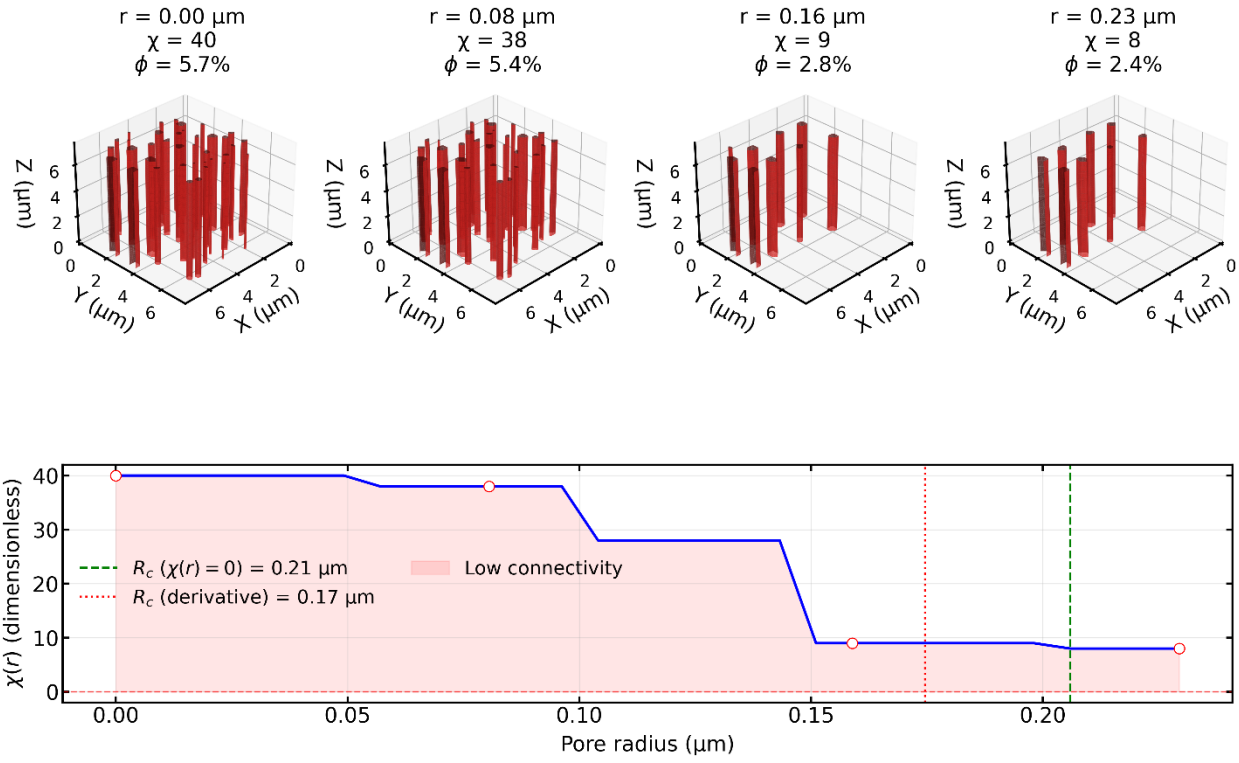

Figure 8. EPC analysis for BPC. Top panels: evolution of the 3D pore structure during morphological opening at increasing radii. Bottom panel: connectivity function

$\chi(r)$ remaining positive throughout until it reaches zero. Zero-crossing criterion corresponds with the largest capillary.

Figure 8 shows the opening process and the connectivity function $\chi(r)$, which decreased from 40 to 8 in discrete steps. Transitions at r = 0.08 and 0.16 μm corresponded to removal of small and medium capillaries. The derivative criterion yielded R_c= 0.17 μm, corresponding to the PSD mode; however, without lateral connections and with all remaining capillaries providing independent flow paths, no unique percolation threshold exists.

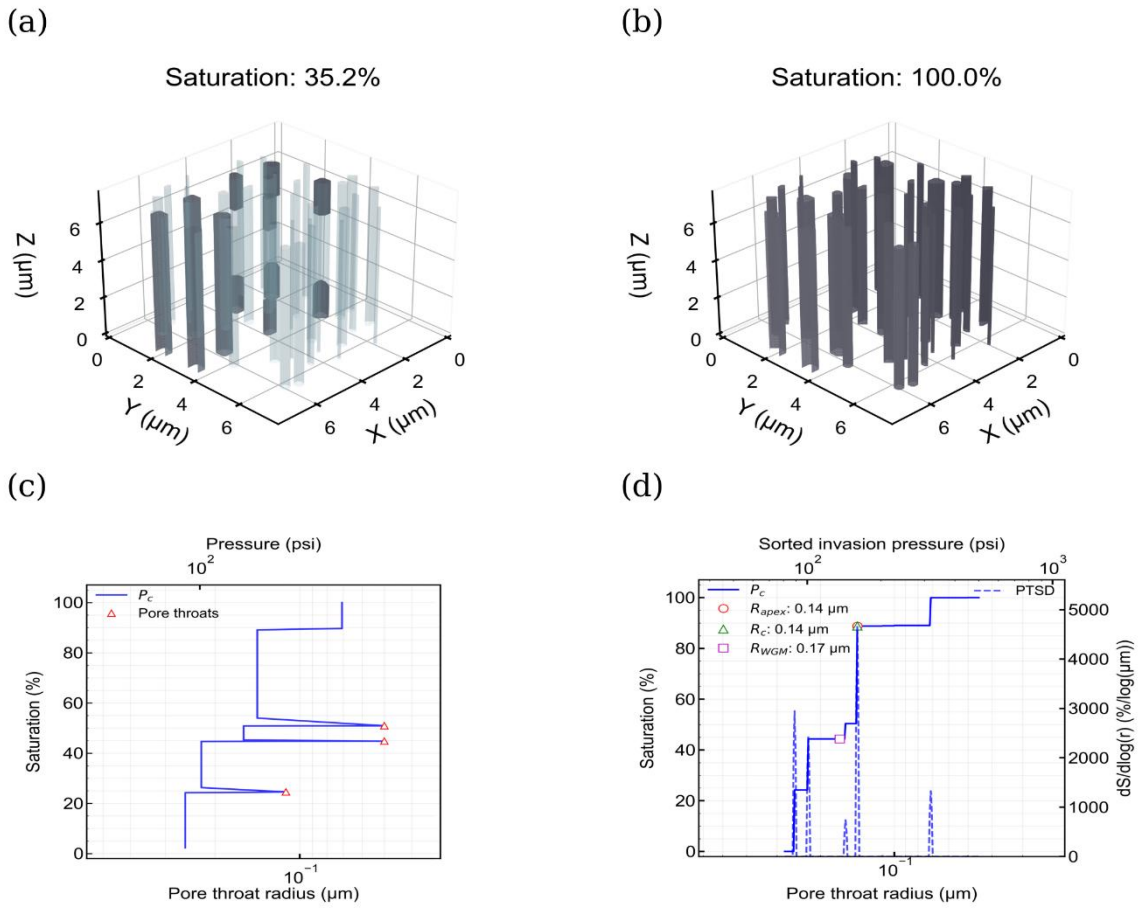

Figure 9. QBIP invasion characterization for BPC. (a–b) 3D visualization of volume-controlled invasion at two saturation states. (c) Volume-controlled invasion curve.

(d) Pressure-controlled reconstruction: invasion events sorted by decreasing radius, with PTSD overlay (dashed): R_{apex}= 0.14 μm, R_c= 0.14 μm, and R_{WGM}= 0.17 μm. QBIP analysis determined R_c despite the disconnected structure (Figure 9). Invasion proceeded by capillary radius (Figure 9a). Volume-controlled invasion (Figure 9c) showed three plateaus corresponding to the three capillary radius classes. Pressure-controlled analysis (Figure 9d) showed entry events at radii of 0.08, 0.15, and 0.25 μm. Both modal and apex methods yielded R_c = 0.14 μm; R_{WGM} = 0.17 μm.

Method comparison for BPC is asymmetric: EPC cannot determine a percolation threshold because χ_0= 40 (positive) prevents zero-crossing identification. The derivative criterion returned 0.17 μm, which exceeded the design modal radius (0.15 μm) by 13.3%. QBIP determined R_c = 0.14 μm, 6.7% below it (0.15 μm).

The 0.03 μm difference between the EPC derivative and QBIP does not represent disagreement on the percolation threshold: BPC percolates by design, but the EPC derivative identifies the PSD mode, and the zero-crossing value (0.21 μm) corresponds to the radius at which $\chi(r)$ reaches zero—the disappearance of the largest capillary—not a topological transition.

4.2. Multidirectional channels

The MDC structure consisted of orthogonal channels with diagonal connections.

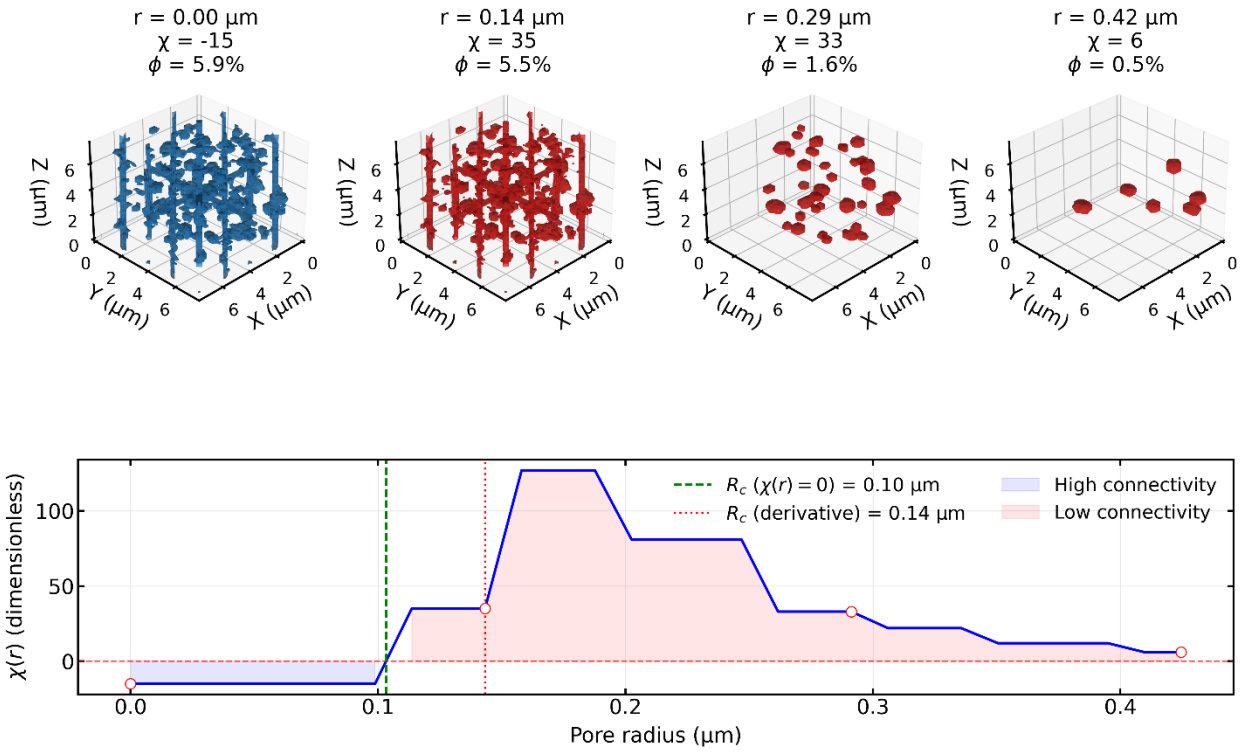

524

525 **Figure 10.** EPC analysis for MDC. Top panels: pore structure at opening radii of
526 0.00, 0.14, 0.29, and 0.42 µm. Bottom panel: connectivity function $\chi(r)$ starting at
527 $\chi_0 = -15$, with zero-crossing at $R_c = 0.10$ µm and derivative criterion at $R_c = 0.14$
528 µm.

529 Figure 10 shows the connectivity function, which transitioned from $\chi_0 = -15$ to
530 positive values. The zero-crossing occurred at R_c = 0.10 µm. The derivative criterion
531 yielded R_c = 0.14 µm. The 0.04 µm difference between the criteria indicated that the
532 topological transition and the maximum rate of change occur at distinct radii in this
533 structure.

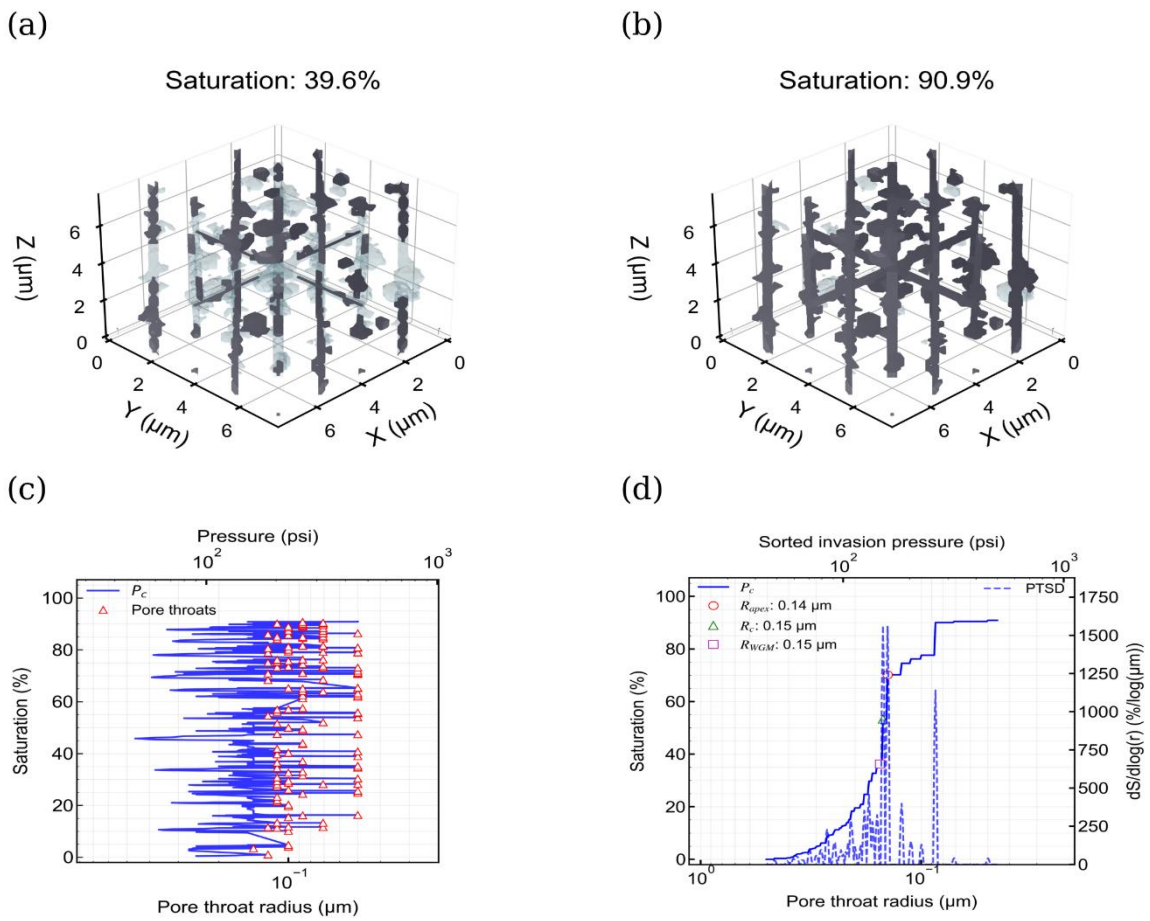

534

535 **Figure 11.** QBIP invasion characterization for MDC. (a–b) 3D visualization of
536 volume-controlled invasion at two saturation states. (c) Volume-controlled invasion
537 curve. (d) Pressure-controlled reconstruction: invasion events sorted by decreasing
538 radius, with PTSD overlay (dashed): $R_{apex} = 0.14$ μm, R_c= 0.15 μm, and $R_{WGM} =$
539 0.15 μm.

540 QBIP analysis of MDC (Figure 11) showed channel invasion (Figure 11a). The
541 maximum invaded saturation reached 90.9% (Figure 11b); the remaining porosity
542 corresponds to isolated pores inaccessible to the invading phase. Volume-controlled
543 invasion (Figure 11c) displayed step-wise saturation increases. Pressure-controlled

analysis (Figure 11d) yielded R_c = 0.15 µm from modal analysis; R_{apex} = 0.14 µm and R_{WGM} = 0.15 µm.

Method comparison for MDC showed 0.04 µm internal EPC divergence between zero-crossing (R_c = 0.10 µm) and derivative (R_c = 0.14 µm) criteria. QBIP yielded R_c = 0.15 µm. Relative to the design modal radius, the zero-crossing deviated by 0%, the derivative by 40%, and QBIP by 50%. The zero-crossing coincided with the design modal radius; QBIP yielded a larger value, consistent with the dilation applied in Section 3.1.

4.3. Hierarchical tree network

The HTN structure consisted of branching paths generated via a minimum spanning tree algorithm.

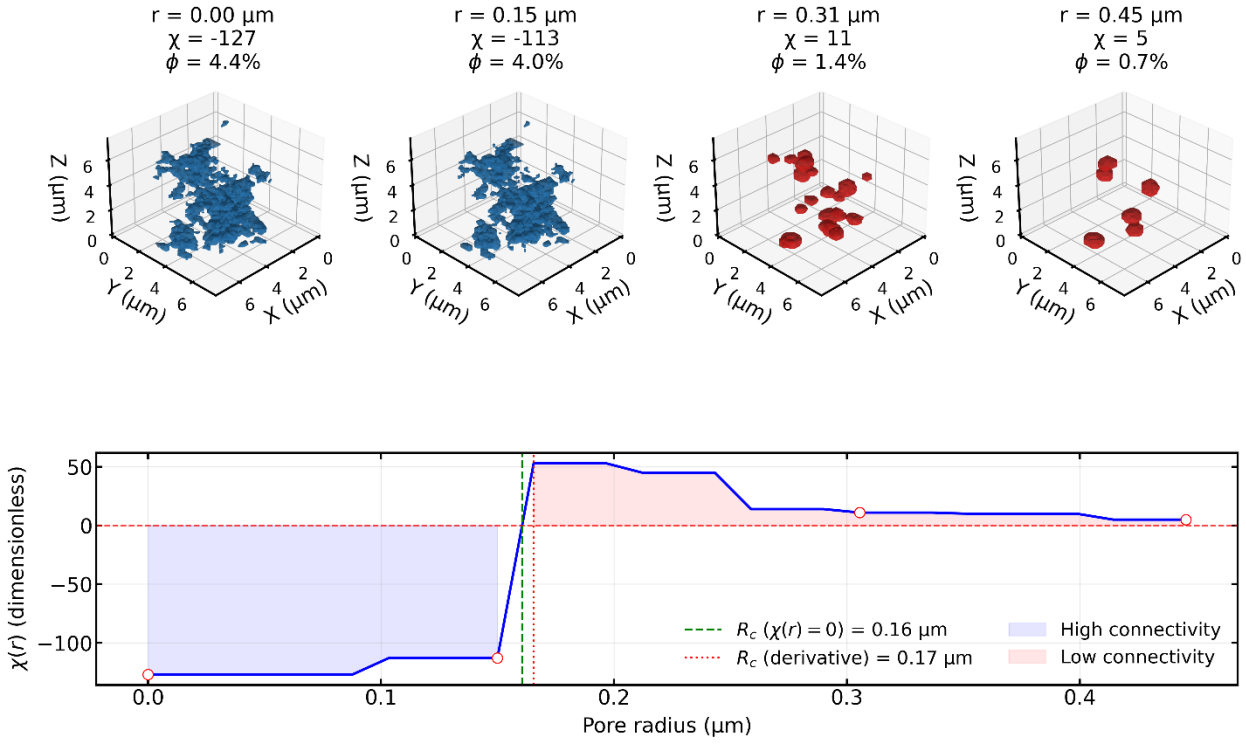

Figure 12. EPC analysis for HTN. Top panels: pore structure at opening radii of 0.00, 0.15, 0.31, and 0.45 µm. Bottom panel: connectivity function starting at $\chi_0 = -127$. Zero-crossing at $R_c = 0.16$ µm; derivative criterion at $R_c = 0.17$ µm.

Figure 12 shows the connectivity function, which transitioned from χ_0 = −127 to positive values, with the zero-crossing between r = 0.15 and 0.17 µm. The zero-crossing occurred at R_c = 0.16 µm; the derivative criterion yielded R_c = 0.17 µm (0.01 µm internal divergence).

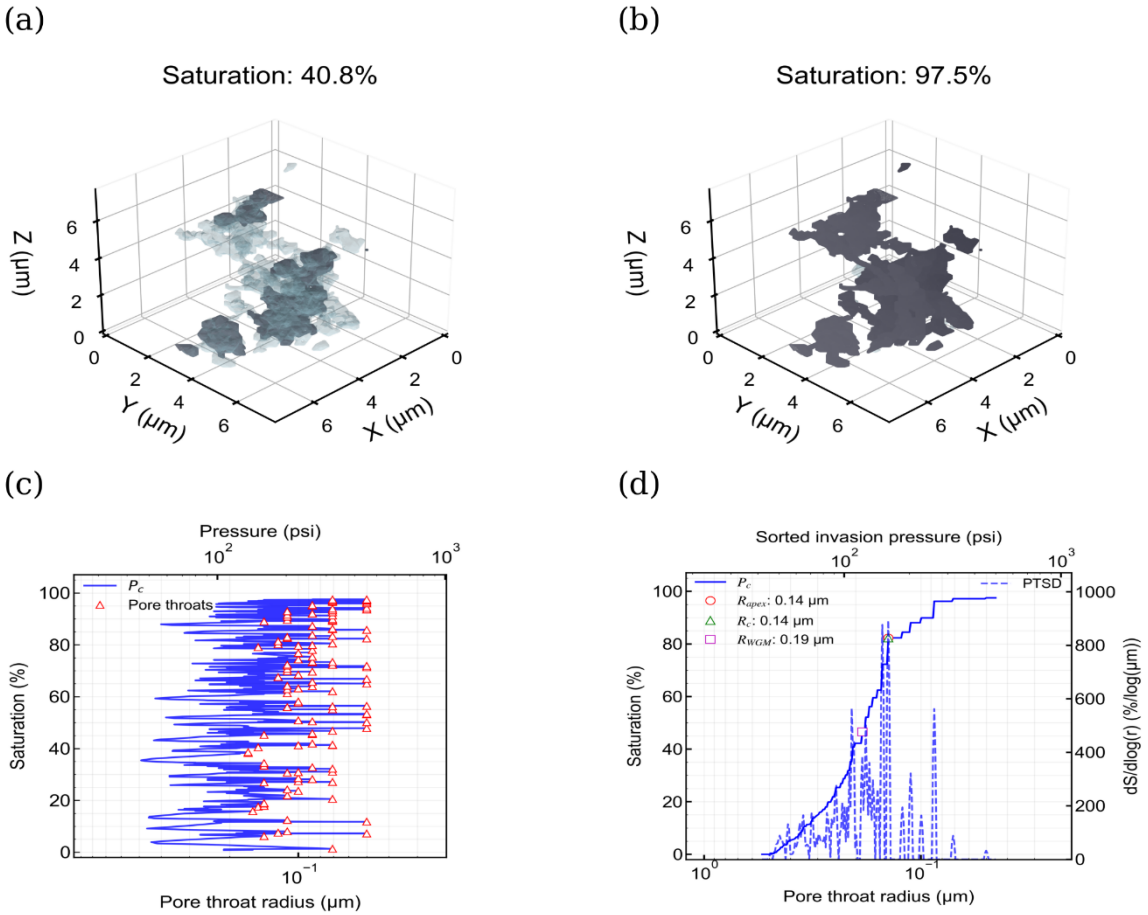

Figure 13. QBIP invasion characterization for HTN. (a–b) 3D visualization of volume-controlled invasion at two saturation states. (c) Volume-controlled invasion curve. (d)

Pressure-controlled reconstruction: invasion events sorted by decreasing radius, with PTSD overlay (dashed): $R_c = 0.14$ μm (modal), $R_{apex} = 0.14$ μm, $R_{WGM} = 0.19$ μm.

QBIP analysis of HTN (Figure 13) showed hierarchical invasion through the primary branches (Figure 13a). Volume-controlled invasion (Figure 13c) displayed irregular saturation jumps at branch connections. Pressure-controlled analysis (Figure 13d) yielded R_c = 0.14 μm from modal analysis; R_{apex} = 0.14 μm and R_{WGM} = 0.19 μm.

Method comparison for HTN showed 0.01 μm internal EPC divergence between zero-crossing (R_c = 0.16 μm) and derivative (R_c = 0.17 μm) criteria. Relative to the design modal radius (0.10 μm), the zero-crossing deviated by 60%, the derivative by 70%, and QBIP by 40%. Both EPC criteria exceeded QBIP (R_c = 0.14 μm) by 0.02 μm and 0.03 μm, respectively. The pore-throat radii at branch junctions are distributed across a range that morphological opening and invasion percolation sample differently; in this structure, the topological transition detected by EPC does not coincide with the percolation threshold.

4.4. Degree-constrained network

The DCN structure assigned size-dependent coordination numbers (Z = 2–6) to each pore.

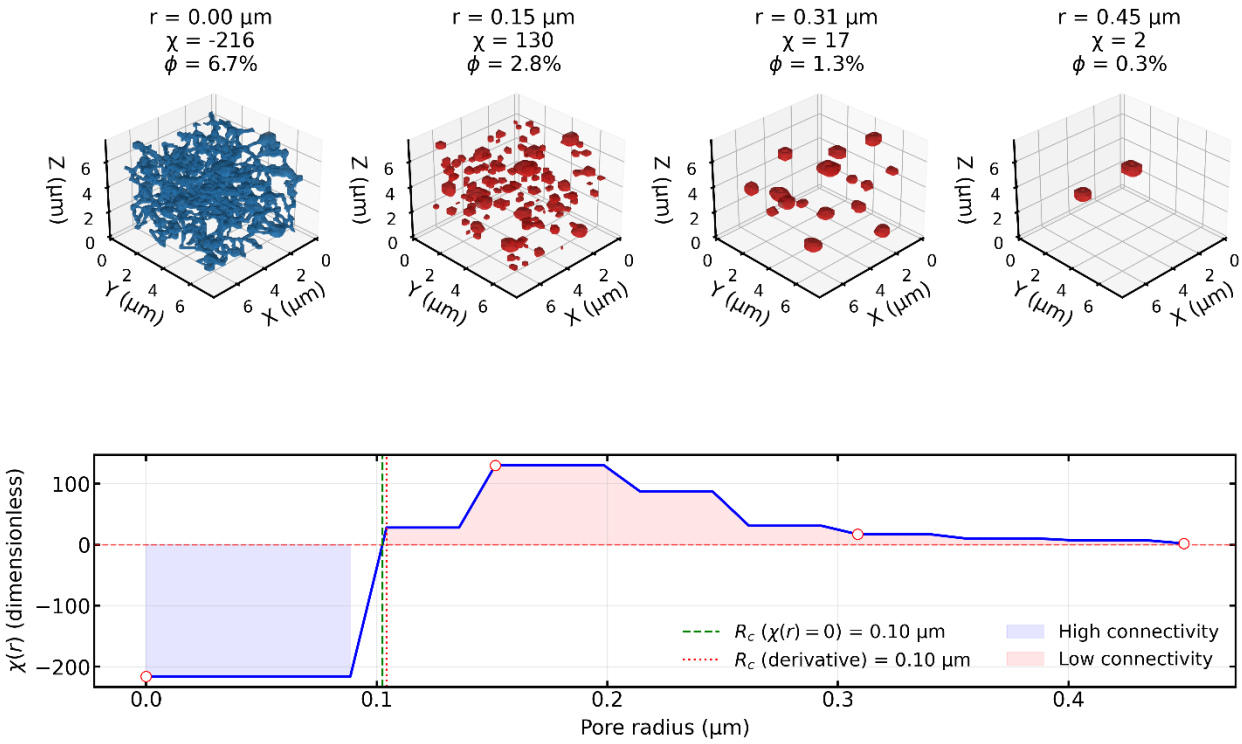

584

585 **Figure 14.** EPC analysis for DCN. Top panels: 3D pore structure at opening radii of
586 0.00, 0.15, 0.31, and 0.45 µm. Bottom panel: connectivity function with $\chi_0 = -216$,
587 zero-crossing at $R_c = 0.10$ µm and derivative criterion at $R_c = 0.10$ µm. Transition
588 from $\chi = -216$ to $\chi = 130$ occurs within 0.05 µm range.

589 Figure 14 shows the connectivity function, which transitioned from χ_0 = −216 to
590 positive values, reaching χ = 130 within the 0.10–0.15 µm range. The zero-crossing
591 occurred at R_c = 0.10 µm; the derivative criterion yielded R_c = 0.10 µm (0% internal
592 divergence).

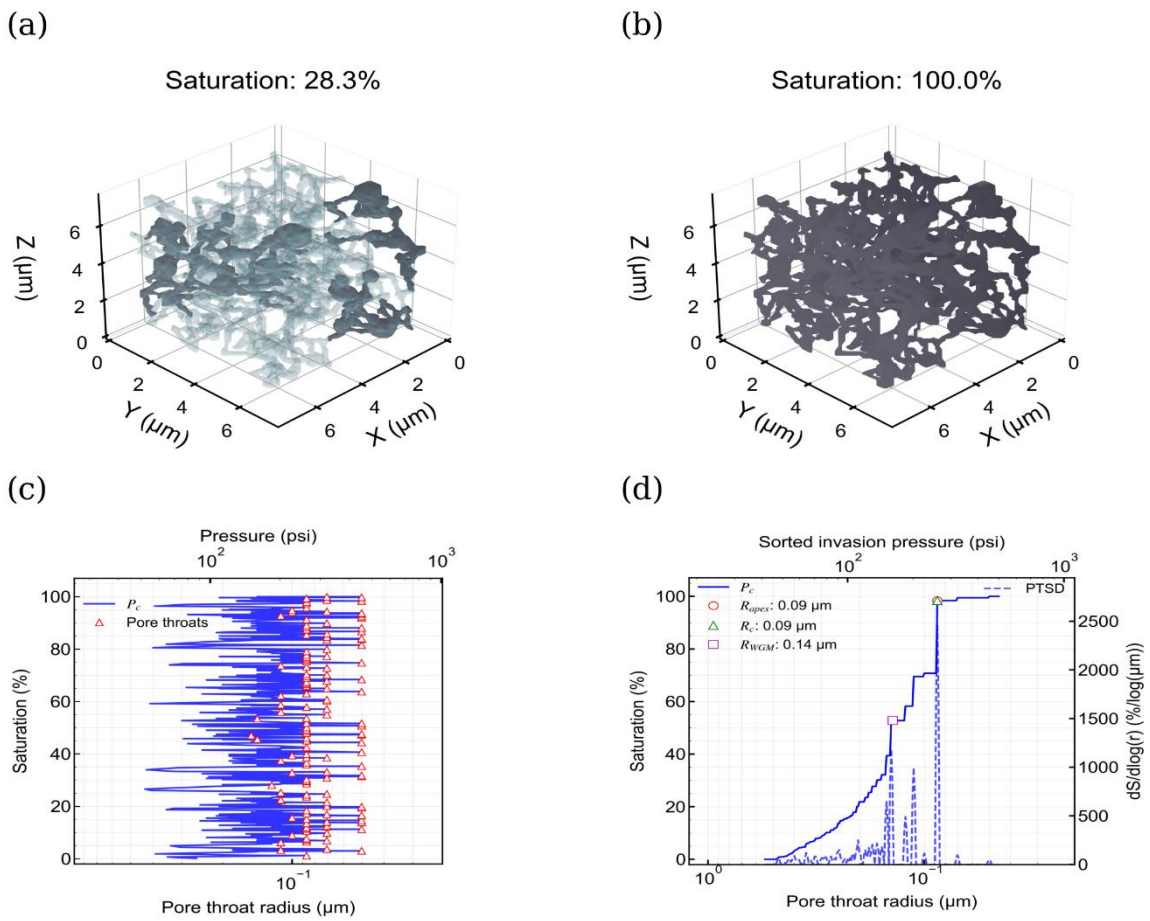

593

594 **Figure 15.** QBIP invasion characterization for DCN. (a–b) 3D visualization of
595 volume-controlled invasion at two saturation states. (c) Volume-controlled invasion
596 curve. (d) Pressure-controlled reconstruction: invasion events sorted by decreasing
597 radius, with PTSD overlay (dashed): $R_c = R_{apex} = 0.09$ μm, $R_{WGM} = 0.14$ μm.

598 QBIP analysis of DCN (Figure 15) showed invasion through the coordinated network
599 (Figure 15a). Volume-controlled invasion (Figure 15c) displayed irregular saturation
600 jumps. Pressure-controlled analysis (Figure 15d) yielded R_c = R_{apex} = 0.09 μm; R_{WGM}
601 = 0.14 μm.

Method comparison for DCN showed 0% internal EPC divergence: both criteria yielded R_c = 0.10 μm. QBIP yielded R_c = 0.09 μm, resulting in 0.01 μm difference for both criteria. Relative to the design modal radius (0.10 μm), both EPC criteria deviated by 0% and QBIP by 10%. This is the smallest deviation among all SPS. The controlled coordination numbers (Z = 2–6) produce a narrow pore-throat distribution around the design modal radius; under these conditions, the topological transition detected by EPC and the percolation threshold identified by QBIP converge toward the same radius. The 0.01 μm residual difference may reflect the discrete nature of voxelized opening radii in EPC versus the continuous invasion front in QBIP.

4.5. Summary of results

Table 2 compiles R_c determinations, R_{WGM}, and percentage deviations ($\%dev$) across all SPS. The percentage deviation relative to the design modal radius is defined as:

$$\%dev = \frac{|R_c - r_{\text{design}}|}{r_{\text{design}}} * 100. \quad (13)$$

Table 2. Critical radius determination across synthetic porous structures. Percentage deviations calculated relative to the design modal radius.

SPS	χ_0	R_c EPC* (μm)	R_c QBIP (μm)	R_{WGM} (μm)	$\%dev$ EPC*	$\%dev$ QBIP
BPC	40	0.21†/0.17†	0.14	0.17	40†/13.3†	6.7
MDC	−15	0.10/0.14	0.15	0.15	0/40	50
HTN	−127	0.16/0.17	0.14	0.19	60/70	40
DCN	−216	0.10/0.10	0.09	0.14	0/0	10

†BPC: EPC does not detect a percolation threshold (χ_0 > 0). Zero-crossing corresponds to disappearance of the largest capillary; derivative identifies PSD mode. Differences are nominal. All percentages use the design modal radius as denominator. *EPC zero-crossing / derivative criteria.

The percentage deviations in Table 2 show that method performance varies across topologies. Three patterns emerge. First, QBIP determined R_c in all four structures (deviations of 6.7–50% from design modal radii), whereas EPC zero-crossing is restricted to structures with negative initial connectivity; in BPC, the zero-crossing and derivative values are nominal because no percolation threshold exists. Second, no single EPC criterion was uniformly closer to either the design modal radius or the QBIP value: the EPC derivative was within 0.01 μm of QBIP in MDC and DCN but diverged by 0.03 μm in HTN, while the zero-crossing was within 0.02 μm in HTN but diverged by 0.05 μm in MDC. Third, internal EPC divergence (difference between zero-crossing and derivative criteria) decreases with increasing connectivity: 0.04 μm (MDC, χ_0 = −15), 0.01 μm (HTN, χ_0 = −127), and 0 μm (DCN, χ_0= −216); in highly connected structures, the two EPC criteria converge, and the EPC–QBIP gap narrows. Both methods identified R_c within the same order of magnitude as the design modal radii (0.10–0.15 μm); the binary dilation applied during SPS generation accounts for the larger deviations in MDC and HTN. R_{WGM} exceeded R_c in all four SPS (0.14–0.19 μm), consistent with its definition as the weighted mean of the invaded pore-throat spectrum.

5. Conclusions

This study presents the first comparison of EPC and QBIP methods for R_c determination across four SPS with topologies ranging from disconnected to highly connected. The results yield the following conclusions:

1. QBIP determined R_c in all four structures regardless of connectivity. EPC zero-crossing is restricted to $\chi_0 < 0$; in disconnected structures, even when individual flow paths connect opposite faces, the zero-crossing criterion cannot be applied. The derivative criterion returns a value in all cases, but in disconnected structures it identifies the PSD mode, not a percolation threshold.

2. No single EPC criterion was uniformly closer to either the design modal radius or the QBIP value across all topologies. The relative ranking between zero-crossing and derivative criteria depends on network topology.

3. Internal EPC divergence (difference between zero-crossing and derivative criteria) decreases with increasing connectivity. In highly connected structures, the two EPC criteria converge, and the EPC–QBIP gap narrows.

4. Both methods identified R_c values within the same order of magnitude as the design modal radii, despite morphological operations during SPS generation. R_{WGM} consistently exceeded R_c in all SPS, consistent with its definition as the weighted mean of the invaded pore-throat spectrum.

Based on these results, method selection depends on the initial EPC value of the medium: if $\chi_0 < 0$ is confirmed, EPC provides R_c without invasion simulation, with deviations that depend on network topology; if χ_0 is unknown or positive, QBIP is required. When both methods are applicable, their agreement serves as a consistency check on R_c determination.

The comparison is limited to four SPS with fixed voxel resolution and a single dilation iteration; sensitivity to resolution and binning parameters remains to be evaluated. Future work should extend this comparison to natural rocks imaged by micro-CT and to stochastic pore models—such as Boolean, Cox, and Gaussian random field models—which provide intermediate topological complexity between the controlled structures studied here and natural pore networks. Gaussian models are of particular interest because the EPC can be computed analytically rather than estimated from voxelized images. Experimental validation against pressure-based experiments-derived R_c values in natural rocks and the evaluation of how uncertainty in R_c propagates to permeability estimation through Eq. 1 remain open directions.

Acknowledgments

The authors Franco-Villegas, Nieto-Rivero, and Morales-Chávez thank the SECIHTI (Secretaría de Ciencia, Humanidades, Tecnología e Innovación) for its financial support and the Graduate Program of the IMP for its academic guidance, and the anonymous reviewers whose comments helped improve the quality of this manuscript.

Code Availability

The source codes are available at the link: https://github.com/MFV-PS/EPC-QBIP-Rc under the MIT License. The repository includes both EPC and QBIP implementations as Jupyter notebooks with example synthetic porous structures.

References

1. Aguilar-Madera, C. G., Flores-Cano, J. V., Matías-Pérez, V., Briones-Carrillo, J. A., & Velasco-Tapia, F. (2020). Computing the permeability and Forchheimer tensor of porous rocks via closure problems and digital images. *Advances in Water Resources*, *142*, 103616. https://doi.org/10.1016/j.advwatres.2020.103616

2. Ahmed, U., Crary, S. F., & Coates, G. R. (1991). Permeability Estimation: The Various Sources and Their Interrelationships. *Journal of Petroleum Technology*, *43*(05), 578–587. https://doi.org/10.2118/19604-PA

3. Amann-Hildenbrand, A., Bertier, P., Busch, A., & Krooss, B. M. (2013). Experimental investigation of the sealing capacity of generic clay-rich caprocks. *International Journal of Greenhouse Gas Control*, *19*, 620–641. https://doi.org/10.1016/j.ijggc.2013.01.040

4. Andrä, H., Combaret, N., Dvorkin, J., Glatt, E., Han, J., Kabel, M., Keehm, Y., Krzikalla, F., Lee, M., Madonna, C., Marsh, M., Mukerji, T., Saenger, E. H., Sain, R., Saxena, N., Ricker, S., Wiegmann, A., & Zhan, X. (2013a). Digital rock physics benchmarks—Part I: Imaging and segmentation. *Computers & Geosciences*, *50*, 25–32. https://doi.org/10.1016/j.cageo.2012.09.005

5. Andrä, H., Combaret, N., Dvorkin, J., Glatt, E., Han, J., Kabel, M., Keehm, Y., Krzikalla, F., Lee, M., Madonna, C., Marsh, M., Mukerji, T., Saenger, E. H., Sain, R., Saxena, N., Ricker, S., Wiegmann, A., & Zhan, X. (2013b). Digital rock physics benchmarks—part II: Computing effective properties.

Computers & Geosciences, *50*, 33–43. https://doi.org/10.1016/j.cageo.2012.09.008

6. Armstrong, R. T., McClure, J. E., Robins, V., Liu, Z., Arns, C. H., Schlüter, S., & Berg, S. (2019). Porous Media Characterization Using Minkowski Functionals: Theories, Applications and Future Directions. *Transport in Porous Media*, *130*(1), 305–335. https://doi.org/10.1007/s11242-018-1201-4

7. Arns, C. H. (2004). A comparison of pore size distributions derived by NMR and X-ray-CT techniques. *Physica A: Statistical Mechanics and Its Applications*, *339*(1), 159–165. https://doi.org/10.1016/j.physa.2004.03.033

8. Arns, C., Knackstedt, M., & Martys, N. (2005). Cross-property correlations and permeability estimation in sandstone. *Physical Review E*, *72*(4), 046304. https://doi.org/10.1103/PhysRevE.72.046304

9. Bernabé, Y. (1995). The transport properties of networks of cracks and pores. *Journal of Geophysical Research*, *100*(B3), 4231–4241. https://doi.org/10.1029/94JB02986

10. Bernabé, Y., Li, M., & Maineult, A. (2010). Permeability and pore connectivity: A new model based on network simulations. *J. Geophys. Res.*, *115*(B10), 2010JB007444. https://doi.org/10.1029/2010JB007444

11. Bernabé, Y., Li, M., Tang, Y.-B., & Evans, B. (2016). Pore Space Connectivity and the Transport Properties of Rocks. *Oil Gas Sci. Technol. – Rev. IFP Energies Nouvelles*, *71*(4), 50. https://doi.org/10.2516/ogst/2015037

12. Blunt, M. J., Bijeljic, B., Dong, H., Gharbi, O., Iglauer, S., Mostaghimi, P., Paluszny, A., & Pentland, C. (2013). Pore-scale imaging and modelling. *Advances in Water Resources*, *51*, 197–216. https://doi.org/10.1016/j.advwatres.2012.03.003

13. Bultreys, T., De Boever, W., & Cnudde, V. (2016). Imaging and image-based fluid transport modeling at the pore scale in geological materials: A practical introduction to the current state-of-the-art. *Earth-Science Reviews*, *155*, 93–128. https://doi.org/10.1016/j.earscirev.2016.02.001

14. Chaniot, J., Moreaud, M., Sorbier, L., Becker, J.-M., & Fournel, T. (2022). Scalable morphological accessibility of complex microstructures. *Computational Materials Science*, *203*, 111062. https://doi.org/10.1016/j.commatsci.2021.111062

15. Comisky, J. T., Newsham, K. E., Rushing, J. A., & Blasingame, T. A. (2007). A Comparative Study of Capillary-Pressure-Based Empirical Models for Estimating Absolute Permeability in Tight Gas Sands. *SPE Annual Technical Conference and Exhibition*, *SPE-110050-MS*. https://doi.org/10.2118/110050-MS

16. Daigle, H. (2016). Application of critical path analysis for permeability prediction in natural porous media. *Advances in Water Resources*, *96*, 43–54. https://doi.org/10.1016/j.advwatres.2016.06.016

17. Dastidar, R., Sondergeld, C. H., & Rai, C. S. (2007). An Improved Empirical Permeability Estimator From Mercury Injection For Tight Clastic Rocks. *Petrophysics - The SPWLA Journal*, *48*(03).

18. Davudov, D., Moghanloo, R. G., & Zhang, Y. (2020). Interplay between pore connectivity and permeability in shale sample. *International Journal of Coal Geology*, *220*, 103427. https://doi.org/10.1016/j.coal.2020.103427

19. Franco-Villegas, M., Coconi-Morales, E., Nieto-Rivero, C. J. T., Valdiviezo-Mijangos, Oscar. C., & Fuentes-Cruz, G. (2025). Permeability estimation using Poiseuille models: A case study on comparative analysis of characteristic radii in tight rocks. *Geofísica Internacional*, *64*(4), 1731–1750. https://doi.org/10.22201/igeof.2954436xe.2025.64.4.1877

20. Ghanbarian, B., Hunt, A. G., Ewing, R. P., & Sahimi, M. (2013). Tortuosity in Porous Media: A Critical Review. *Soil Science Society of America Journal*, *77*(5), 1461–1477. https://doi.org/10.2136/sssaj2012.0435

21. Ghomeshi, S., Kryuchkov, S., & Kantzas, A. (2018). An investigation into the effects of pore connectivity on T2 NMR relaxation. *Journal of Magnetic Resonance*, *289*, 79–91. https://doi.org/10.1016/j.jmr.2018.02.007

22. Giesche, H. (2006). Mercury Porosimetry: A General (Practical) Overview. *Particle & Particle Systems Characterization*, *23*(1), 9–19. https://doi.org/10.1002/ppsc.200601009

23. Goral, J., & Deo, M. (2020). Nanofabrication of synthetic nanoporous geomaterials: From nanoscale-resolution 3D imaging to nano-3D-printed

digital (shale) rock. *Sci Rep*, *10*(1), 21596. https://doi.org/10.1038/s41598-020-78467-z

24. Gostick, J., Khan, Z., Tranter, T., Kok, M., Agnaou, M., Sadeghi, M., & Jervis, R. (2019). PoreSpy: A Python Toolkit for Quantitative Analysis of Porous Media Images. *Journal of Open Source Software*, *4*(37), 1296. https://doi.org/10.21105/joss.01296

25. Gostick, J. T., Misaghian, N., Irannezhad, A., & Zhao, B. (2024). A computationally efficient queue-based algorithm for simulating volume-controlled drainage under the influence of gravity on volumetric images of porous materials. *Advances in Water Resources*, *193*, 104799. https://doi.org/10.1016/j.advwatres.2024.104799

26. Gostick, J. T., Misaghian, N., Yang, J., & Boek, E. S. (2022). Simulating volume-controlled invasion of a non-wetting fluid in volumetric images using basic image processing tools. *Computers & Geosciences*, *158*, 104978. https://doi.org/10.1016/j.cageo.2021.104978

27. Guibert, R., Horgue, P., Debenest, G., & Quintard, M. (2016). A Comparison of Various Methods for the Numerical Evaluation of Porous Media Permeability Tensors from Pore-Scale Geometry. *Mathematical Geosciences*, *48*(3), 329–347. https://doi.org/10.1007/s11004-015-9587-9

28. Guo, B.-E., Xiao, N., Martyushev, D., & Zhao, Z. (2024). Deep learning-based pore network generation: Numerical insights into pore geometry effects on

microstructural fluid flow behaviors of unconventional resources. *Energy*, *294*, 130990. https://doi.org/10.1016/j.energy.2024.130990

29. Hildenbrand, A., Schlömer, S., & Krooss, B. M. (2002). Gas breakthrough experiments on fine-grained sedimentary rocks. *Geofluids*, *2*(1), 3–23. https://doi.org/10.1046/j.1468-8123.2002.00031.x

30. Hilpert, M., & Miller, C. T. (2001). Pore-morphology-based simulation of drainage in totally wetting porous media. *Advances in Water Resources*, *24*(3), 243–255. https://doi.org/10.1016/S0309-1708(00)00056-7

31. Hou, X., Qi, S., Guo, S., Zhang, L., Ma, L., Li, Y., Wang, Y., Li, T., & Peng, J. (2025). 3D pore structure characteristics of intact and compacted loess and their controls on hydraulic permeability. *Journal of Hydrology*, *663*, 134126. https://doi.org/10.1016/j.jhydrol.2025.134126

32. Huang, H., Li, R., Xiong, F., Hu, H., Sun, W., Jiang, Z., Chen, L., & Wu, L. (2020). A method to probe the pore-throat structure of tight reservoirs based on low-field NMR: Insights from a cylindrical pore model. *Marine and Petroleum Geology*, *117*, 104344. https://doi.org/10.1016/j.marpetgeo.2020.104344

33. Hunt, A. G. (2001). Applications of percolation theory to porous media with distributed local conductances. *Advances in Water Resources*, *24*(3), 279–307. https://doi.org/10.1016/S0309-1708(00)00058-0

34. Jiang, Z., Van Dijke, M. I. J., Sorbie, K. S., & Couples, G. D. (2013). Representation of multiscale heterogeneity via multiscale pore networks:

812 Representation of Multiscale Heterogeneity. *Water Resources Research*,
813 *49*(9), 5437–5449. https://doi.org/10.1002/wrcr.20304

814 35. Jivkov, A. P., Hollis, C., Etiese, F., McDonald, S. A., & Withers, P. J. (2013).
815 A novel architecture for pore network modelling with applications to
816 permeability of porous media. *Journal of Hydrology*, *486*, 246–258.
817 https://doi.org/10.1016/j.jhydrol.2013.01.045

818 36. Kaczmarek, Ł., Wejrzanowski, T., Skibiński, J., Maksimczuk, M., & Krzyżak,
819 A. (2017). High-resolution computed microtomography for the
820 characterization of a diffusion tensor imaging phantom. *Acta Geophysica*,
821 *65*(1), 259–268. https://doi.org/10.1007/s11600-017-0021-1

822 37. Katz, A. J., & Thompson, A. H. (1986). Quantitative prediction of permeability
823 in porous rock. *Physical Review B*, *34*(11), 8179–8181.
824 https://doi.org/10.1103/PhysRevB.34.8179

825 38. Katz, A. J., & Thompson, A. H. (1987). Prediction of rock electrical
826 conductivity from mercury injection measurements. *J. Geophys. Res.*, *92*(B1),
827 599–607. https://doi.org/10.1029/JB092iB01p00599

828 39. Kelly, S., El-Sobky, H., Torres-Verdín, C., & Balhoff, M. T. (2015). Assessing
829 the utility of FIB-SEM images for shale digital rock physics. *Advances in Water*
830 *Resources*, *95*, 302–316. https://doi.org/10.1016/j.advwatres.2015.06.010

831 40. Knackstedt, M., & Paterson, L. (2009). Invasion Percolation. In M. Sahimi &
832 A. G. Hunt (Eds.), *Complex Media and Percolation Theory* (pp. 175–190).
833 Springer US. https://doi.org/10.1007/978-1-0716-1457-0_294

41. León Y León, C. A. (1998). New perspectives in mercury porosimetry. *Advances in Colloid and Interface Science*, *76–77*, 341–372. https://doi.org/10.1016/s0001-8686(98)00052-9

42. Li, B., Liu, R., & Jiang, Y. (2016). A multiple fractal model for estimating permeability of dual-porosity media. *Journal of Hydrology*, *540*, 659–669. https://doi.org/10.1016/j.jhydrol.2016.06.059

43. Luo, M., Glover, P. W. J., Zhao, P., & Li, D. (2020). 3D digital rock modeling of the fractal properties of pore structures. *Marine and Petroleum Geology*, *122*, 104706. https://doi.org/10.1016/j.marpetgeo.2020.104706

44. Ma, T., Ding, M., Zhang, F., Cui, C., Cui, S., & Wang, Y. (2025). Dynamic Evolution of Pore Structures in Unconsolidated Sandstone Reservoir during High-Rate Polymer Flooding. *Energy & Fuels*, *39*(18), 8473–8481. https://doi.org/10.1021/acs.energyfuels.5c01014

45. McPhee, C., Reed, J., & Zubizarreta, I. (2015). Routine Core Analysis. In *Developments in Petroleum Science* (Vol. 64, pp. 181–268). Elsevier. https://doi.org/10.1016/B978-0-444-63533-4.00005-6

46. Morales-Chávez, S., Valdez-Grijalva, M. A., Díaz-Viera, M. A., Lucas-Oliveira, E., & Bonagamba, T. J. (2025). A mathematical model of NMR transverse relaxation for pore size distribution estimation in porous media. *Journal of Magnetic Resonance*, *379*, 107922. https://doi.org/10.1016/j.jmr.2025.107922

47. Mosser, L., Dubrule, O., & Blunt, M. J. (2017). Reconstruction of 3D porous media using generative adversarial neural networks. *Physical Review E*, *96*(4), 043309. https://doi.org/10.1103/PhysRevE.96.043309

48. Mostaghimi, P., Blunt, M. J., & Bijeljic, B. (2013). Computations of Absolute Permeability on Micro-CT Images. *Math Geosci*, *45*(1), 103–125. https://doi.org/10.1007/s11004-012-9431-4

49. Narsilio, G. A., Buzzi, O., Fityus, S., Yun, T. S., & Smith, D. W. (2009). Upscaling of Navier–Stokes equations in porous media: Theoretical, numerical and experimental approach. *Computers and Geotechnics*, *36*(7), 1200–1206. https://doi.org/10.1016/j.compgeo.2009.05.006

50. Nelson, P. H. (2009). Pore-throat sizes in sandstones, tight sandstones, and shales. *Bulletin*, *93*(3), 329–340. https://doi.org/10.1306/10240808059

51. Nishiyama, N., & Yokoyama, T. (2017). Permeability of porous media: Role of the critical pore size: Critical Pore Size-Permeability Relation. *J. Geophys. Res. Solid Earth*, *122*(9), 6955–6971. https://doi.org/10.1002/2016JB013793

52. Okabe, H., & Blunt, M. J. (2005). Pore space reconstruction using multiple-point statistics. *Journal of Petroleum Science and Engineering*, *46*(1), 121–137. https://doi.org/10.1016/j.petrol.2004.08.002

53. Patmonoaji, A., Tsuji, K., & Suekane, T. (2020). Pore-throat characterization of unconsolidated porous media using watershed-segmentation algorithm. *Powder Technology*, *362*, 635–644. https://doi.org/10.1016/j.powtec.2019.12.026

54. Pittman, E. D. (1992). Relationship of porosity and permeability to various parameters derived from mercury injection-capillary pressure curves for sandstone. *AAPG Bulletin*, *76*(2), 191–198.

55. Quan, F., Zhang, Y., Lu, W., Wei, C., Dai, X., & Qin, Z. (2025). Multifractal Characterization of Full-Scale Pore Structure in Middle-High-Rank Coal Reservoirs: Implications for Permeability Modeling in Western Guizhou–Eastern Yunnan Basin. *Processes*, *13*(6). https://doi.org/10.3390/pr13061927

56. Rabbani, A., Ayatollahi, S., Kharrat, R., & Dashti, N. (2016). Estimation of 3-D pore network coordination number of rocks from watershed segmentation of a single 2-D image. *Advances in Water Resources*, *94*, 264–277. https://doi.org/10.1016/j.advwatres.2016.05.020

57. Raeini, A. Q., Bijeljic, B., & Blunt, M. J. (2017). Generalized network modeling: Network extraction as a coarse-scale discretization of the void space of porous media. *Phys. Rev. E*, *96*(1), 013312. https://doi.org/10.1103/PhysRevE.96.013312

58. Rashid, F., Glover, P. W. J., Lorinczi, P., Hussein, D., Collier, R., & Lawrence, J. (2015). Permeability prediction in tight carbonate rocks using capillary pressure measurements. *Marine and Petroleum Geology*, *68*, 536–550. https://doi.org/10.1016/j.marpetgeo.2015.10.005

59. Rezaee, R., Saeedi, A., & Clennell, B. (2012). Tight gas sands permeability estimation from mercury injection capillary pressure and nuclear magnetic

resonance data. *Journal of Petroleum Science and Engineering*, *88–89*, 92–99. https://doi.org/10.1016/j.petrol.2011.12.014

60. Robins, V., Saadatfar, M., Delgado-Friedrichs, O., & Sheppard, A. P. (2016). Percolating length scales from topological persistence analysis of micro-CT images of porous materials. *Water Resources Research*, *52*(1), 315–329. https://doi.org/10.1002/2015WR017937

61. Roth, S., Biswal, B., Afshar, G., Held, R. J., Øren, P.-E., Inge Berge, L., & Hilfer, R. (2011). Continuum-based rock model of a reservoir dolostone with four orders of magnitude in pore sizes. *AAPG Bulletin*, *95*(6), 925–940. https://doi.org/10.1306/12031010092

62. Saha Ray, S. (2013). *Graph Theory with Algorithms and its Applications: In Applied Science and Technology*. Springer India. https://doi.org/10.1007/978-81-322-0750-4

63. Sahimi, M. (2011). *Flow and Transport in Porous Media and Fractured Rock: From Classical Methods to Modern Approaches* (1st ed.). Wiley. https://doi.org/10.1002/9783527636693

64. Santos, J. E., Gigliotti, A., Bihani, A., Landry, C., Hesse, M. A., Pyrcz, M. J., & Prodanović, M. (2022). MPLBM-UT: Multiphase LBM library for permeable media analysis. *SoftwareX*, *18*, 101097. https://doi.org/10.1016/j.softx.2022.101097

65. Spivey, J. P., & Lee, W. J. (2013). *Applied Well Test Interpretation*. Society of Petroleum Engineers. https://doi.org/10.2118/9781613993071

66. van der Walt, S., Schönberger, J.L., Nunez-Iglesias, J., Boulogne, F., Warner, J.D., Yager, N., Gouillart, E., Yu, T., and the scikit-image contributors. (2014). scikit-image: image processing in Python. *PeerJ*, 2, e453. https://doi.org/10.7717/peerj.453

67. Verri, I., Della Torre, A., Montenegro, G., Onorati, A., Duca, S., Mora, C. A., Radaelli, F., & Trombin, G. (2017). Development of a Digital Rock Physics workflow for the analysis of sandstones and tight rocks. *Journal of Petroleum Science and Engineering*, *156*, 790–800. https://doi.org/10.1016/j.petrol.2017.06.053

68. Vogel, H. J. (1997). Morphological determination of pore connectivity as a function of pore size using serial sections. European Journal of Soil Science, 48(3), 365-377.

69. Vogel, H.-J. (2002). Topological Characterization of Porous Media. In K. Mecke & D. Stoyan (Eds.), *Morphology of Condensed Matter* (Vol. 600, pp. 75–92). Springer Berlin Heidelberg. https://doi.org/10.1007/3-540-45782-8_3

70. Vogel, H.-J., Weller, U., & Schlüter, S. (2010). Quantification of soil structure based on Minkowski functions. *Computers & Geosciences*, *36*(10), 1236–1245. https://doi.org/10.1016/j.cageo.2010.03.007

71. Washburn, E. W. (1921). The Dynamics of Capillary Flow. *Phys. Rev.*, *17*(3), 273–283. https://doi.org/10.1103/PhysRev.17.273

941 72. Wilkinson, D., & Willemsen, J. F. (1983). Invasion percolation: A new form of
942 percolation theory. *Journal of Physics A: Mathematical and General*, *16*(14),
943 3365–3376. https://doi.org/10.1088/0305-4470/16/14/028

944 73. Xu, H., Fan, Y., Hu, F., Li, C., Yu, J., Liu, Z., & Wang, F. (2019).
945 Characterization of Pore Throat Size Distribution in Tight Sandstones with
946 Nuclear Magnetic Resonance and High-Pressure Mercury Intrusion.
947 *Energies*, *12*(8). https://doi.org/10.3390/en12081528

948 74. Zhang, L., Liu, J., He, X., Feng, F., Li, W., Wang, M., Zhu, W., & Zhu, Y.
949 (2025). Fractal Characteristics and Influencing Factors of Pore Structure in
950 Tight Sandstone: A Case Study from Chang 6 Member of the Southwestern
951 Yishan Slope. *Processes*, *13*(4). https://doi.org/10.3390/pr13040988

952 75. Zhang, Y., Xiao, L., Liao, G., & Song, Y.-Q. (2016). Direct correlation of
953 diffusion and pore size distributions with low field NMR. *Journal of Magnetic*
954 *Resonance*, *269*, 196–202. https://doi.org/10.1016/j.jmr.2016.06.013

955 76. Zhao, Y. (2019). Estimating critical path analysis on digital topology of the
956 connectivity of pore media. *Multimedia Tools and Applications*, *78*(1), 1165–
957 1180. https://doi.org/10.1007/s11042-018-6587-z

958 77. Zheng, S., Yao, Y., Liu, D., Cai, Y., & Liu, Y. (2018). Characterizations of full-
959 scale pore size distribution, porosity and permeability of coals: A novel
960 methodology by nuclear magnetic resonance and fractal analysis theory.
961 *International Journal of Coal Geology*, *196*, 148–158.
962 https://doi.org/10.1016/j.coal.2018.07.008

78. Zhu, W., Yu, W., & Chen, Y. (2012). Digital core modeling from irregular grains. *Journal of Applied Geophysics*, *85*, 37–42. https://doi.org/10.1016/j.jappgeo.2012.06.013